

## Article

# Constraints on the Genesis of the Shuangwang Gold Deposit in Qinling Orogen, Central China: Evidence from In Situ Trace Element and Sulfur Isotope

Junjie Yang<sup>1</sup>, Xingke Yang<sup>1,2,\*</sup>, Jianbo Li<sup>1</sup>, Hujun He<sup>1,2</sup> , Huixia Chao<sup>1,2</sup> and Pengfei Yi<sup>1,3,4</sup><sup>1</sup> School of Earth Science and Resources, Chang'an University, Xi'an 710054, China<sup>2</sup> Key Laboratory of Western Mineral Resources and Geological Engineering, Ministry of Education, Xi'an 710054, China<sup>3</sup> Shaanxi Institute of Geological Survey, Xi'an 710054, China<sup>4</sup> Shaanxi Mineral Resources and Geological Survey, Xi'an 710054, China

\* Correspondence: xky6105@chd.edu.cn

**Abstract:** The Shuangwang gold deposit, with more than 70 tons of Au, is located in the Fengxian-Taibai ore concentration area in the Qinling Orogen of central China, hosted in a Northwest-trending breccia belt. Fragments of the breccia body are cemented by ankerite, albite, quartz, calcite, and pyrite. Four metallogenic stages are identified in mineral paragenesis: quartz-albite, ankerite-pyrite-albite, pyrite-quartz-calcite, and fluorite-anhydrite. Pyrite, as the main gold-bearing mineral, was formed in the syn-ore and post-ore stages, which are analyzed for trace elements. The experimental results show that Au (0.02 to 11.68 ppm), As (198.45 to 5502.86 ppm), Ag (0.00 to 1.56 ppm), Co (0.02 to 1002.75 ppm), Ni (0.15 to 646.30 ppm), Cu (0.00 to 64.76 ppm), Sb (0.00 to 4.67 ppm), Zn (0.23 to 260.59 ppm), Pb (0.00 to 10.42 ppm), Se (0.00 to 386.24 ppm), and Bi (0.00 to 47.72 ppm) are enriched in syn-ore pyrite much more than in post-ore pyrite, especially arsenic. The high arsenic content and rapid crystallization of pyrite may be the main reasons for precipitation of gold.  $\delta^{34}\text{S}_{\text{V-CDT}}$  values of pyrite formed in stage II (Py<sub>II</sub>) vary from 11.1 to 15.2‰ (mean = 12.9‰), while those for pyrite formed in stage III (Py<sub>III</sub>) vary from 11.1 to 13.5‰ (mean = 12.0‰). In situ sulfur isotope analysis indicates that sulfur of the Shuangwang deposit comes from the wallrock, mixed with sulfur from magma.

**Keywords:** pyrite; trace element; sulfur isotope; Shuangwang; Qinling Orogen

**Citation:** Yang, J.; Yang, X.; Li, J.; He, H.; Chao, H.; Yi, P. Constraints on the Genesis of the Shuangwang Gold Deposit in Qinling Orogen, Central China: Evidence from In Situ Trace Element and Sulfur Isotope. *Minerals* **2022**, *12*, 995. <https://doi.org/10.3390/min12080995>

Academic Editor: Léo Afraneo Hartmann

Received: 16 June 2022

Accepted: 4 August 2022

Published: 6 August 2022

**Publisher's Note:** MDPI stays neutral with regard to jurisdictional claims in published maps and institutional affiliations.



**Copyright:** © 2022 by the authors. Licensee MDPI, Basel, Switzerland. This article is an open access article distributed under the terms and conditions of the Creative Commons Attribution (CC BY) license (<https://creativecommons.org/licenses/by/4.0/>).

## 1. Introduction

The Qinling Orogenic Belt (QOB), as one of the most important gold regions in China, hosts more than 50 gold deposits. In recent years, Chinese geologists have reviewed the Western Qinling gold deposits, including their distribution, classification, geological characteristics, and ore-forming process [1–3].

For the Shuangwang gold deposit, located in the Fengxian-Taibai (Feng-Tai) ore concentration area, gold is mainly produced in the cement of the breccia body. The boundaries between orebodies and breccia bodies are usually delineated by assay results. For this reason, scholars have carried out a lot of related research, including ore-forming fluid and stable isotopes [4–7], Iron and Magnesium isotopes [8], He-Ar isotopes [9], and mineral characteristics [10–12]. Due to its particularity, there is still a great controversy regarding the genetic type, including the orogenic type [1], Carlin-like type [3], Carlin or Carlin-like type [2], cryptoexplosive breccia type [4], and so on.

This paper identifies two generations of pyrite, which is consistent with previous studies, indicating that there is still one pyrite crystallization in the later stage of mineralization, which does not contain gold. We study the trace element composition and sulfur isotopes in the two generations of pyrite, as well as distinguishing differences in their elemental compositions and discuss the possible causes for them. Our results provide insights into the

ore-forming fluid and allows for assessment of the source of sulfur, providing geochemical evidence for study of the genesis of the Shuangwang gold deposit.

### 2. Geological Setting

The Qinling Orogenic Belt (QOB) is located between the North China Craton and Yangtze Craton and has undergone complex tectonic evolution [13–15]. It can be divided into the North Qinling Block (NQB) and South Qinling Block (SQB) by the Shangdan suture. The Feng-Tai ore concentration area is located in the north margin of the SQB (Figure 1), and is rich in mineral resources of lead, zinc, gold, copper, and so on. The proven gold reserves are over 125 tons, while lead and zinc metal reserves are nearly 5 million tons in the area [16]. The Feng-tai ore concentration area is mainly exposed in the Devonian unit, which is a set of low-grade metamorphic littoral-neritic clastic rock-carbonate formations, followed by a small amount of Carboniferous–Triassic unit. The Devonian unit, from bottom to top, includes the Middle Devonian Macaogou Formation, the Middle Devonian Gudaoling Formation, the Upper Devonian Xinghongpu Formation, and the Upper Devonian Jiuliping Formation. Pb–Zn deposits are mainly in the contact zone of the Xinghongpu and Gudaoling Formations, and gold deposits in the area are mainly in the Xinghongpu Formation (Figure 2). The overall structure of the area is a complex fold, mainly in the axial direction of NWW. There are many faults in the area. The intrusive rocks in the area include Baoji pluton, Taibai pluton, and Ningshan composite pluton, which have the characteristics of multiple periods and types. The Xiba pluton is the northwestern part of the Ningshan composite pluton.

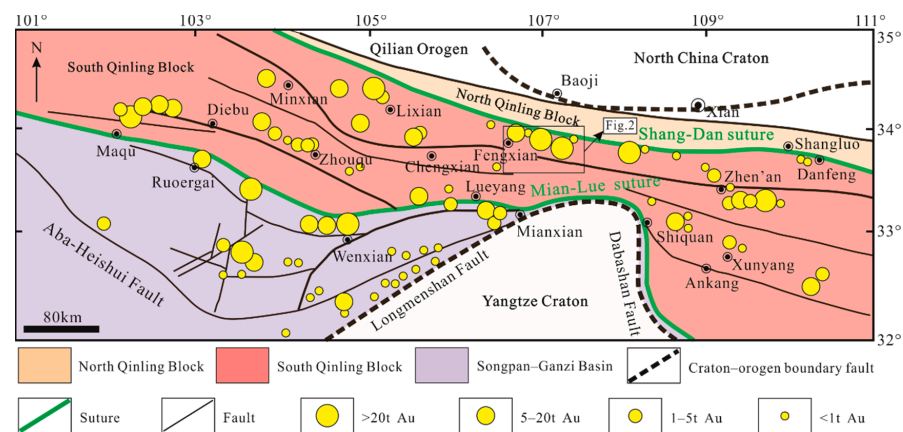


Figure 1. Simplified geological map of the western Qinling Orogen with the location of gold deposits (modified from [2,17]).

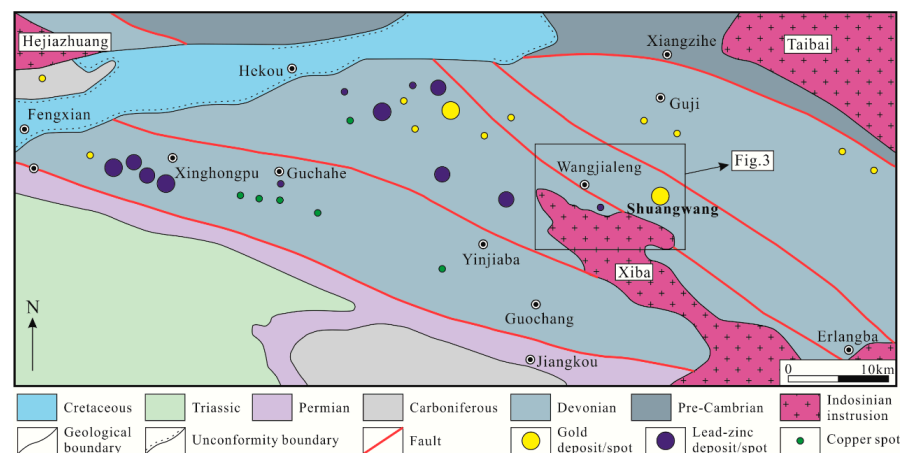
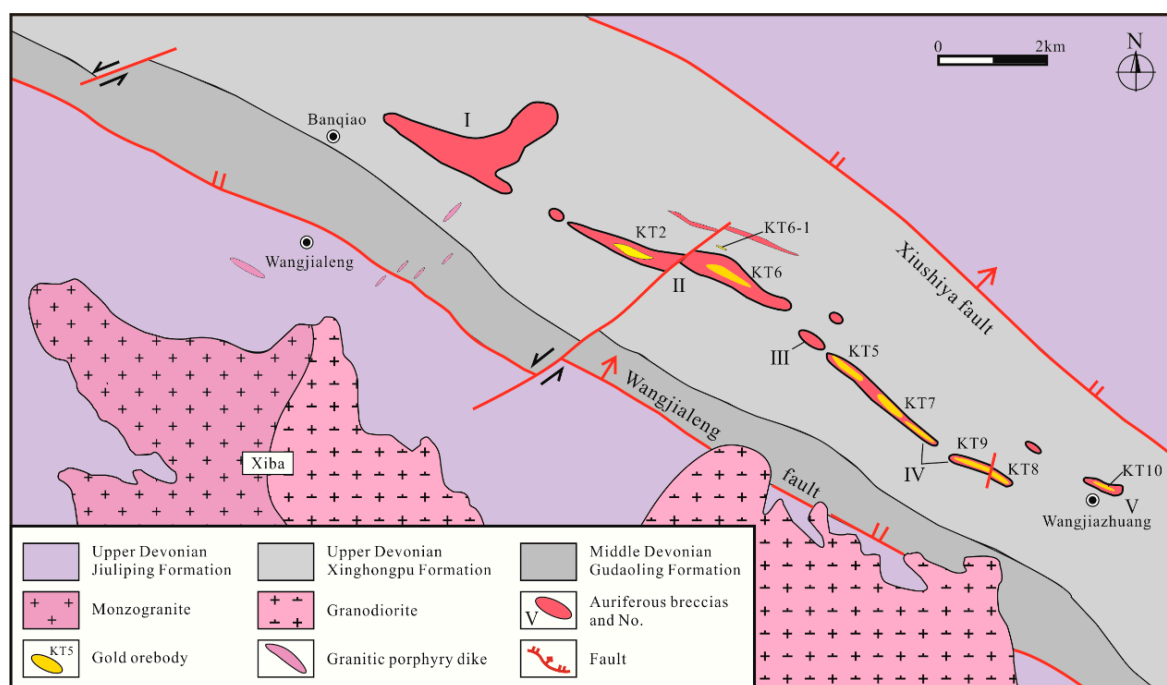


Figure 2. Sketch map of geology and deposits in the Feng-Tai ore concentration area (modified after [18,19]).

### 3. Ore Deposit Geology

The Devonian unit are exposed in the mining area, including the Gudaoling Fm., Xinghongpu Fm., and Jiuliping Fm. The Xinghongpu Fm. is main ore-bearing stratum, which is composed of meta-siltstone, silty sericite slate, siltstone, and sodic rock. NW direction faults include the Wangjialeng and Xiushiya faults, which are in the south and north of the ore district, respectively (Figure 3). Strata and orebodies were staggered by NE direction faults, which are formed after the mineralized period (Figure 3). The fold in the ore district is the Shiziling anticline, with the axis direction of NW. The Gudaoling Fm. exists in the core of the anticline, and the Xinghongpu Fm. exists in the north flank of the anticline. The pluton of Xiba intruded into the southern wing of the anticline, resulting in an absence of strata. The Xiba pluton, the largest intrusive rock, was formed through two stages of magmatism, forming granodiorite and monzonitic granite. According to previous research results, the pluton invaded in 214–222 Ma [9,20–22]. Dykes, including granite porphyry, imandrite, and lamprophyre, formed in 213–219 Ma [9,23].



**Figure 3.** Simplified geological map of the Shuangwang gold deposit (modified from [24]).

Orebodies of the Shuangwang Gold deposit are mainly hosted in the breccia body of the Upper Devonian Xinghongpu Fm. Breccia bodies occur as lenticular form in plane, with sac-like or thick-plate form in section. Breccia is mainly albitized silty slate, with a small amount of marble and cements including ankerite, albite, quartz, calcite, and pyrite. There are differences in cements between different positions or orebodies. When the gold in the breccia body reaches industrial grade, the breccia body is the orebody. Eight orebodies, including KT2, KT6, KT6-1, KT5, KT7, KT9, KT8, and KT10, are delineated from west to east (Figure 3), and the gold reserves have reached 70 t. The ore of KT8 and KT9 showed ankerite cemented breccia, KT6 showed albite cemented breccia, and KT6-1 and KT2 showed pyrite cemented breccia. Au mainly occurs in pyrite in cement. The main alteration types in the Shuangwang gold ore district are albitization, dolomitization, and carbonatization, followed by silicification.

Based on the spatial relationship between orebody and wallrock, mineralization characteristics, ore fabric, wallrock alteration, and microscopic observations (see Figures 4 and 5), four metallogenic stages can be identified.

Stage I (pre-ore stage) is characterized by yellowish alteration (albitization) in the strata. This stage formed before the breccia body without mineralization and presents fine veins of quartz and albite entering into albitite (Figure 5A,B).

Stage II (syn-ore stage) shows an ankerite–pyrite–albite assemblage (Figure 5C,D). Gold-bearing pyrite occurs as fine grains, disseminated (Figure 5E,F) in euhedral or subhedral ankerite. Breccia fragments were cemented by ankerite. This is the main ore-forming stage of the mine.

Stage III (post-ore stage) is defined by a pyrite–quartz–calcite stage assemblage (Figure 5G–I). Pyrite without gold occurs as euhedral, medium-coarse grains (Figure 5J) in pyrite aggregates and quartz–calcite veins which cut through the breccia body.

Stage IV (post-ore stage) shows a fluorite–anhydrite assemblage. Mineral filling in the breccia fragments (Figure 5K,L) is formed by low-temperature hydrothermal fluid.



**Figure 4.** (A) Outcrop of the breccia body; (B,C) Transition zone of wallrock alteration; (D) Quartz albitite dike intruding into albitization slate; (E–G) Slate accompanied by partial albitization; (H) Lamprophyre intruding into breccia body; (I,J) Breccia body; (K) Granodiorite of the Xiba pluton.

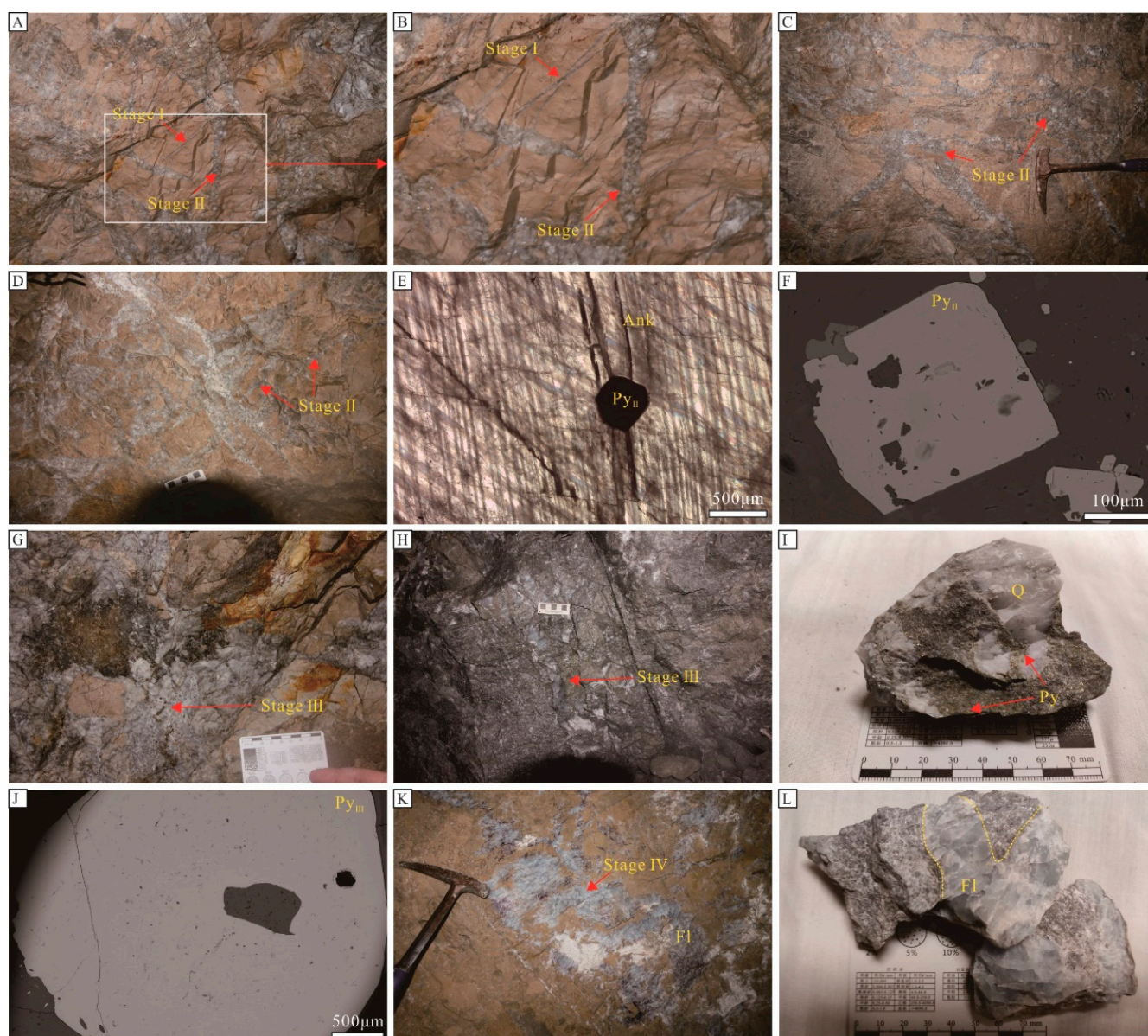


**Figure 5.** Metallogenic stages and characteristics of the Shuangwang gold deposit. (A–D) Fine veins of quartz and albite entered into albitite in stage I and ankerite–pyrite–albite assemblage formed in stage II; (E,F) Gold-bearing pyrite occurs as fine grains, disseminated in euhedral or subhedral ankerite formed in stage II; (G–I) Pyrite–quartz–calcite stage assemblage formed in stage III; (J) Pyrite without gold occurs as euhedral, medium-coarse grain in quartz–calcite veins; (K,L) fluorite–anhydrite assemblage formed in stage IV.

#### 4. Sampling and Analytical Methods

##### 4.1. Samples Description

Samples for experiments were collected from the orebodies of KT5 and KT8. Samples from stage II (syn-ore stage) and stage III (post-ore stage) were selected to make thin sections and were observed by microscope. Two different generations of pyrite were identified, marked as Py<sub>II</sub> and Py<sub>III</sub>.

##### 4.2. In Situ Trace Element Analysis of Pyrite

Trace element analysis of pyrite was conducted by LA-ICP-MS at the Wuhan Sample Solution Analytical Technology Co., Ltd., Wuhan, China. Detailed operating conditions for the laser ablation system, the ICP-MS instrument, and data reduction have been previously

described by Zong et al. [25]. Laser sampling was performed using a GeolasPro laser ablation system consisting of a COMPexPro 102 ArF (Coherent, Santa Clara, CA, USA) excimer laser (wavelength, 193 nm; maximum energy, 200 mJ) and a MicroLas optical system. An Agilent 7700e ICP-MS (Agilent, Santa Clara, CA, USA) instrument was used to acquire ion-signal intensities. Helium was applied as a carrier gas. Argon was used as the make-up gas, which was mixed with the carrier gas by a T-connector before entering the ICP. A “wire” signal smoothing device is included in this laser ablation system [26]. The spot size and frequency of the laser were set to 32  $\mu\text{m}$  and 5 Hz, respectively. Trace element compositions of minerals were calibrated against various reference materials (NIST 610, NIST 612) without use of an internal standard [27]. The sulfide reference material of MASS-1 (USGS) was used as the unknown sample in order to verify the accuracy of the calibration method. Each analysis incorporated a background acquisition of approximately 20–30 s, followed by 50 s of data acquisition from the sample. The Excel-based software ICPMSDataCal (Yongsheng Liu, v11.8, Wuhan, China) was used to perform off-line selection and integration of background and analyzed signals, time-drift correction, and quantitative calibration for trace element analysis [27].

#### 4.3. In Situ Sulfur Isotope Analysis of Pyrite

In situ sulfur isotope analysis of pyrite was carried out at Beijing Createch Testing Technology Co., Ltd., Beijing, China. The instrument was equipped with Photon Machine Analyte G2 laser probe and Nu Plasam HR MC-ICP-MS high-resolution multi-acceptance plasma mass spectrometer. The laser spot beam diameter of the measured element was 30  $\mu\text{m}$ , the frequency was 4 Hz, and the laser energy density was 3.4  $\text{mJ}/\text{cm}^3$  for spot ablation. With helium as the carrier gas, the gas was transported to the ICP-MS at a flow rate of 0.41 L/min. The analysis time for each sample point included 20 s background analysis and 50–60 s continuous laser ablation. The precision of  $\delta^{34}\text{S}$  was found to be better than 0.4‰. The  $\delta^{34}\text{S}$  parameter was normalized to the Vienna Cañon Diablo Troilite (V-CDT) scale [28,29].

## 5. Analytical Results

### 5.1. Pyrite Types

The type of pyrite is closely related to the metallogenic stage. In stage II (syn-ore stage), pyrite (marked as  $\text{Py}_{\text{II}}$ ) is mostly  $\mu\text{m}$ -sized (100–500  $\mu\text{m}$ ), occurs as euhedral or subhedral with pentagonal dodecahedron and octahedron, and is intergrown with ankerite. In stage III (post-ore stage), pyrite (marked as  $\text{Py}_{\text{III}}$ ) coexists with quartz and calcite. The euhedral pyrite, medium-coarse grain (500–2000  $\mu\text{m}$ ), occurs as cube, pentagonal dodecahedron, and octahedron. Compared with  $\text{Py}_{\text{II}}$ , the pyrite in stage III has larger grains, and low gold content. No growth zone was found in the two generations of pyrite, the most obvious difference between them mainly being the size of grains (Figure 5E,J).

### 5.2. In Situ Trace Element

A total of 35 spots were analyzed in the pyrite, including  $\text{Py}_{\text{II}}$  ( $n = 25$ ) and  $\text{Py}_{\text{III}}$  ( $n = 10$ ). Eleven elements were analyzed: Au, As, Ag, Co, Ni, Cu, Sb, Zn, Pb, Se, and Bi. The obtained data are given in Table 1 and illustrated in Figure 6.

Among the analyzed elements in  $\text{Py}_{\text{II}}$ , the elements had highly variable concentrations, ranging from 0.02 to 11.68 ppm for Au, 198.45 to 5502.86 ppm for As, 0.00 to 1.56 ppm for Ag, 0.02 to 1002.75 ppm for Co, 0.15 to 646.30 ppm for Ni, 0.00 to 64.76 ppm for Cu, 0.00 to 4.67 ppm for Sb, 0.23 to 260.59 ppm for Zn, 0.00 to 10.42 ppm for Pb, 0.00 to 386.24 ppm for Se, and 0.00 to 47.72 ppm for Bi. The elemental concentrations in  $\text{Py}_{\text{III}}$  ranged from 0.20 to 2.33 ppm for Au, 0.34 to 16.98 ppm for As, 0.00 to 0.04 ppm for Ag, 0.02 to 79.21 ppm for Co, 0.89 to 686.35 ppm for Ni, 0.00 to 0.42 ppm for Cu, 0.00 to 0.03 ppm for Sb, 0.28 to 1.59 ppm for Zn, 0.00 to 0.07 ppm for Pb, 0.00 to 86.45 ppm for Se, and 0.00 to 0.01 ppm for Bi (see Table 1).

**Table 1.** Trace elements (ppm) in different types of pyrite from the Shuangwang gold deposit.

Mineral	No.	Au	As	Ag	Co	Ni	Cu	Sb	Zn	Pb	Se	Bi
Py <sub>II</sub>	11-1-01	3.28	5502.86	0.00	270.70	262.73	0.21	0.00	1.14	0.00	62.06	0.75
Py <sub>II</sub>	11-1-02	3.75	3312.97	0.00	143.22	126.10	0.19	0.00	0.74	0.00	80.38	10.23
Py <sub>II</sub>	11-1-03	5.03	1354.64	0.02	1002.75	283.44	0.00	0.00	0.74	0.00	30.53	0.09
Py <sub>II</sub>	11-1-04	2.84	918.54	0.00	80.67	103.31	0.14	0.02	0.55	0.00	13.40	0.88
Py <sub>II</sub>	11-1-05	6.99	989.06	0.00	187.83	101.49	0.09	0.00	0.66	0.00	29.49	0.81
Py <sub>II</sub>	11-2-01	9.01	1338.67	0.92	0.02	0.45	0.25	4.67	0.48	5.11	32.24	2.71
Py <sub>II</sub>	11-2-02	3.21	1139.99	0.20	0.24	0.15	0.15	1.21	0.62	2.20	62.07	0.56
Py <sub>II</sub>	11-2-03	1.02	3840.34	0.00	0.02	0.81	0.06	0.01	0.76	0.00	73.13	27.74
Py <sub>II</sub>	11-2-04	0.44	683.97	0.37	7.91	2.66	0.32	0.79	0.40	3.27	70.24	1.64
Py <sub>II</sub>	11-2-05	0.73	2138.59	0.01	0.03	0.45	0.08	0.12	0.38	0.26	1.27	0.14
Py <sub>II</sub>	2-1-01	11.68	1659.42	0.01	28.42	312.66	0.00	0.01	0.23	0.08	28.67	4.56
Py <sub>II</sub>	2-1-02	0.03	1395.53	0.03	12.64	327.93	0.27	0.35	0.53	0.93	9.29	0.32
Py <sub>II</sub>	2-1-03	1.94	634.29	0.00	3.67	223.35	0.00	0.00	0.26	0.00	6.02	47.72
Py <sub>II</sub>	2-1-04	1.32	356.84	0.08	8.09	195.97	64.76	0.07	134.84	0.19	50.08	11.73
Py <sub>II</sub>	2-1-05	0.02	1931.58	0.02	86.38	521.21	9.33	0.12	260.59	0.18	26.33	0.93
Py <sub>II</sub>	2-2-01	0.33	272.19	0.07	2.35	181.68	0.09	0.05	0.58	0.53	60.51	0.00
Py <sub>II</sub>	2-2-02	0.21	1732.37	0.02	0.92	174.65	0.63	0.01	1.17	0.61	14.42	0.00
Py <sub>II</sub>	2-2-03	2.66	406.49	0.32	3.08	308.84	0.19	0.52	0.84	3.64	92.19	0.00
Py <sub>II</sub>	2-2-04	0.55	198.45	0.01	0.35	113.94	2.05	0.62	1.48	1.29	101.22	0.00
Py <sub>II</sub>	2-2-05	1.88	1286.46	0.06	19.26	646.30	0.28	0.01	1.63	0.67	21.31	0.01
Py <sub>II</sub>	2-3-01	0.80	1731.12	0.09	753.73	382.41	0.08	0.18	0.99	0.72	127.57	2.96
Py <sub>II</sub>	2-3-02	0.88	3383.32	0.06	452.63	602.86	0.00	0.04	1.34	0.72	296.39	3.73
Py <sub>II</sub>	2-3-03	9.42	1139.36	1.56	103.24	145.12	1.11	3.96	5.88	10.42	386.24	0.00
Py <sub>II</sub>	2-3-04	2.30	929.25	0.37	20.32	159.79	0.37	0.35	2.30	2.13	0.00	11.51
Py <sub>II</sub>	2-3-05	0.16	2134.92	0.04	52.06	26.37	0.00	0.10	0.87	0.26	105.92	0.13
Py <sub>III</sub>	13-1-01	1.96	0.76	0.00	0.04	0.89	0.00	0.00	0.39	0.02	0.00	0.00
Py <sub>III</sub>	13-1-02	1.42	0.34	0.00	0.02	1.65	0.06	0.00	0.28	0.05	1.96	0.00
Py <sub>III</sub>	13-1-03	0.32	16.98	0.00	0.18	1.70	0.00	0.02	0.72	0.02	13.12	0.00
Py <sub>III</sub>	13-1-04	1.11	2.71	0.00	16.55	225.61	0.24	0.00	0.87	0.07	20.42	0.00
Py <sub>III</sub>	13-1-05	0.50	1.65	0.01	20.80	222.52	0.09	0.00	0.58	0.00	25.45	0.00
Py <sub>III</sub>	13-2-01	0.83	0.53	0.01	0.06	2.08	0.42	0.00	0.68	0.00	0.00	0.00
Py <sub>III</sub>	13-2-02	0.44	1.20	0.00	0.60	13.26	0.00	0.00	1.21	0.00	0.69	0.00
Py <sub>III</sub>	13-2-03	0.20	0.70	0.04	0.24	4.21	0.00	0.00	1.27	0.00	59.66	0.00
Py <sub>III</sub>	13-2-04	2.33	1.36	0.00	0.20	5.00	0.00	0.03	1.21	0.00	86.45	0.00
Py <sub>III</sub>	13-2-05	0.33	7.34	0.01	79.21	686.35	0.04	0.00	1.59	0.00	33.12	0.01

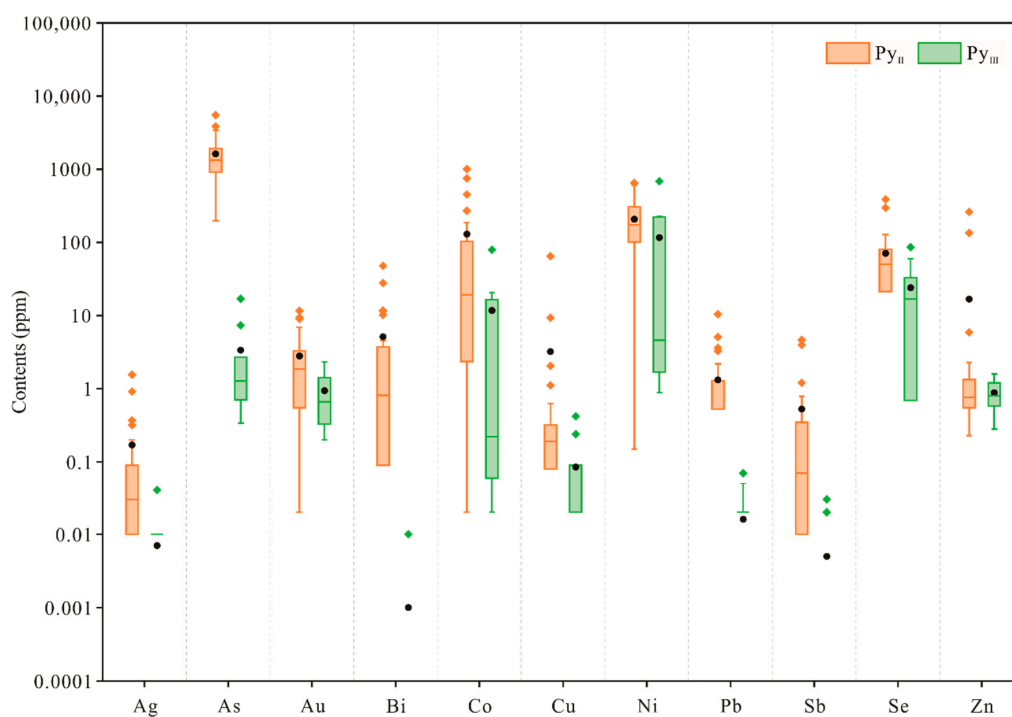


**Figure 6.** Box plot of trace element compositions for pyrite from Shuangwang deposit.

### 5.3. In Situ Sulfur Isotope

The analysis results for the in situ sulfur isotopes are provided in Table 2. The  $\delta^{34}\text{S}_{\text{V-CDT}}$  values of pyrite from the stage II (Py<sub>II</sub>) varied from 11.1 to 15.2‰ (mean = 12.9‰, n = 7), while those in Py<sub>III</sub> varied from 11.1 to 13.5‰ (mean = 12.0‰, n = 3).

**Table 2.** Summary of sulfur isotope results from the Shuangwang gold deposit.

Sample No.	Lithology	Mineral	$\delta^{34}\text{S}_{\text{V-CDT}}$ (‰)	Reference	Sample No.	Lithology	Mineral	$\delta^{34}\text{S}_{\text{V-CDT}}$ (‰)	Reference
14-221	Lamprophyre	Py	4.5	[23]	14-202	Cement	Py	14.9	[23]
T16	Xiba pluton	Py	5.3	[24]	14-232	Cement	Py	9.8	[23]
T17	Xiba pluton	Py	6.1	[24]	SH-90	Cement	Py	10.0	[23]
T52	Xiba pluton	Py	3.8	[24]	14-158	Cement	Py	11.1	[23]
YDZ18	Xiba pluton	Py	4.84	[24]	14-91	Cement	Py	12.1	[23]
T13	Wallrock	Py	10.3	[24]	14-151	Cement	Py	12.9	[23]
T54	Wallrock	Py	5.7	[24]	1100CM32-1	Ore	Py	9.68	[7]
T65	Wallrock	Py	13.5	[24]	1420CM43-1	Ore	Py	13.51	[7]
T66	Wallrock	Py	13.8	[24]	1600CM141-4	Ore	Py	11.93	[7]
T67	Wallrock	Py	9.9	[24]	1600CM75-1	Ore	Py	12.97	[7]
14-57	Pyrite vein	Py	12.7	[23]	2-1550-129-4	Ore	Py	13.94	[7]
14-20	Sericite slate	Py	11.5	[23]	2-1600-187-2	Ore	Py	11.44	[7]
T15	Breccia of albitite	Py	11.6	[24]	2-1600-73-1	Ore	Py	12.86	[7]
T18	Breccia of albitite	Py	8.7	[24]	2-1600-75-1	Ore	Py	12.00	[7]
T53	Breccia of albitite	Py	4.78	[24]	2-3-20-1	Ore	Py	10.77	[7]
T72	Breccia of albitite	Py	9.25	[24]	1330CM13-1	Ore	Py	11.97	[7]
T64	Breccia of albitite	Py	10.78	[24]	4CM18-3	Ore	Py	11.51	[7]
4CM38-2	Ore	Py	9.82	[7]	T71	Ore	Py	9.63	[24]
AHG-5	Ore	Py	14.87	[7]	YDZ1	Ore	Py	10.48	[24]
MGN-2	Ore	Py	9.25	[7]	YDZ2	Ore	Py	7.93	[24]
XMG-3	Ore	Py	13.75	[7]	YDZ3	Ore	Py	11.26	[24]
V-1	Ore	Py	10.83	[7]	YDZ4	Ore	Py	11.54	[24]
V-9	Ore	Py	8.29	[7]	YDZ20	Ore	Py	8.48	[24]
T12	Ore	Py	8.0	[24]	YDZ35	Ore	Py	10.53	[24]
T19	Ore	Py	8.8	[24]	Xishi	Ore	Py	12.91	[24]
T20	Ore	Py	8.3	[24]	Xishi	Ore	Py	12.21	[24]
T24	Ore	Py	14.81	[24]	Xishi	Ore	Py	10.47	[24]
T49	Ore	Py	9.47	[24]	shw-02-DT2-1	Ore	Py <sub>II</sub>	11.5	This study
T51	Ore	Py	9.47	[24]	shw-02-DT2-2	Ore	Py <sub>II</sub>	14.5	This study
T57	Ore	Py	2.6	[24]	shw-02-DT2-4	Ore	Py <sub>II</sub>	12.7	This study
T60	Ore	Py	12.3	[24]	shw-02-DT2-5	Ore	Py <sub>II</sub>	11.7	This study
T63	Ore	Py	4.4	[24]	shw-02-DT2-5	Ore	Py <sub>II</sub>	11.1	This study
T68	Ore	Py	10.84	[24]	shw-08-DT11-1	Ore	Py <sub>II</sub>	15.2	This study
T69	Ore	Py	8.75	[24]	shw-08-DT11-2	Ore	Py <sub>II</sub>	13.4	This study
T70	Ore	Py	10.03	[24]	shw-10-DT13-1	Cement	Py <sub>III</sub>	11.1	This study
14-42	Cement	Anh	26.2	[23]	shw-10-DT13-1	Cement	Py <sub>III</sub>	13.5	This study
14-43	Cement	Anh	24.2	[23]	shw-10-DT13-1	Cement	Py <sub>III</sub>	11.5	This study
14-46	Cement	Anh	25.2	[23]					

## 6. Discussion

### 6.1. Implications of Element Variations

Pyrite is ubiquitous in hydrothermal deposits, especially in gold deposits. As one of the most important gold-bearing minerals, its microstructure and trace element composition are subject to fluid physicochemical conditions and can provide important information about the mineralization process (see, e.g., [30–34]). The trace element characteristics of the Shuangwang gold deposit indicate that the most obvious difference between the two stages of pyrite is the arsenic content (Figure 6, Table 1). The arsenic content in pyrite is closely related to temperature, where low temperatures are more conducive to the enrichment of arsenic [35]. Fluid inclusion data have shown that the temperature of ore-forming fluid decreases gradually (e.g., [4,5,23,36]). If the content of arsenic is sufficient, the pyrite formed in the third stage (i.e., post-ore stage) should be enriched with arsenic as the temperature decreases; this obviously contradicts our experimental results, indicating that the depletion of arsenic in the ore-forming fluid and more stable crystallization environment may be important reasons for the failure of mineralization in the later stage.

There was a visible abundance of microscale inclusions within pyrite (Figure 5F,J). The concentrations of Cu, Pb, and Zn ranged from zero to hundreds of ppm (Table 1). Thus, we may interpret that Cu, Pb, and Zn are distributed in pyrite as (visible or invisible) chalcopyrite, galena, and sphalerite inclusions. These minerals also appear in the mining area [24]. We found that gold has a good correlation with silver (Figure 7), but poor correlations with other elements, indicating that the pyrite contains electrum inclusions.

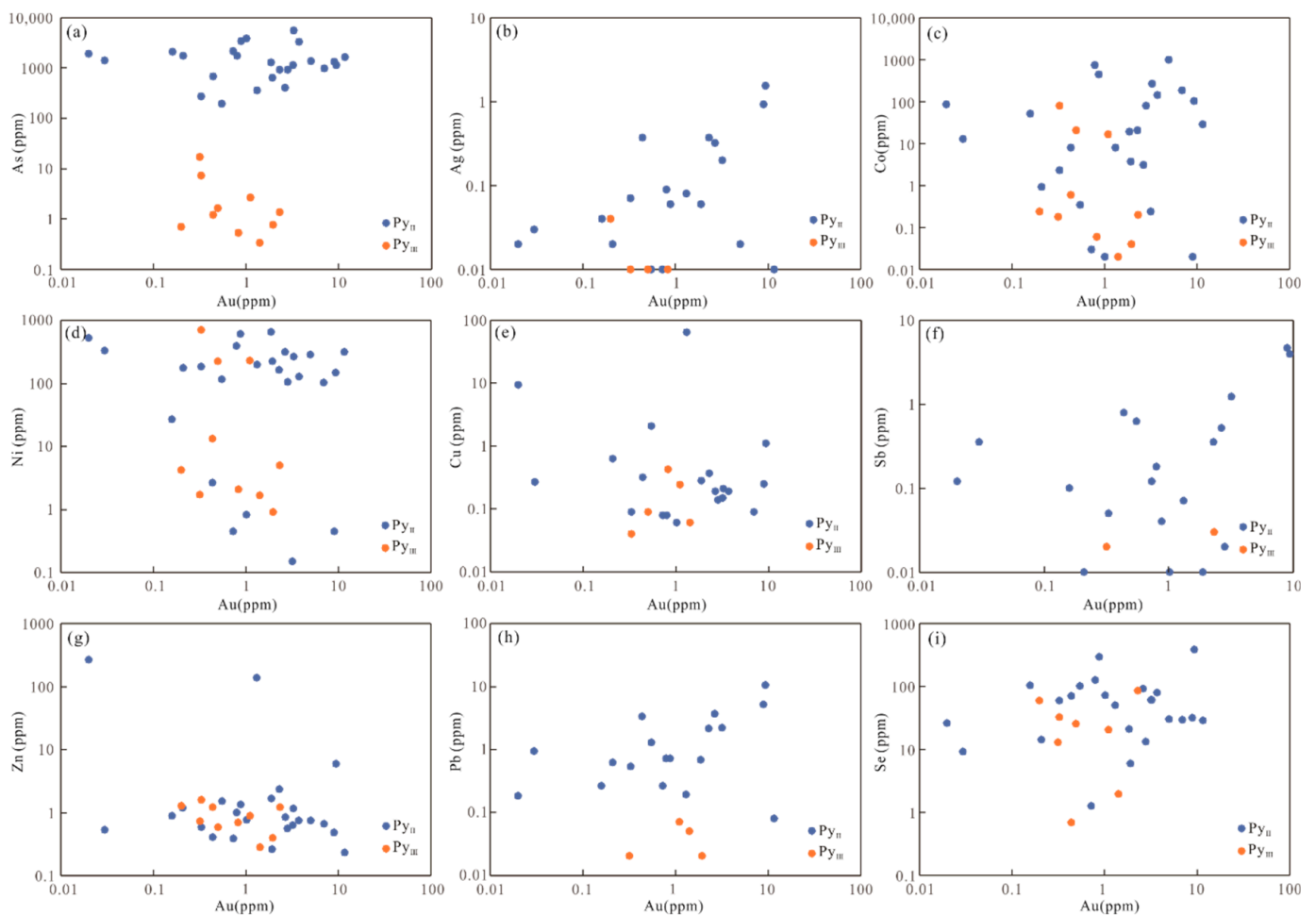


**Figure 7.** Binary plots of (a) As, (b) Ag, (c) Co, (d) Ni, (e) Cu, (f) Sb, (g) Zn, (h) Pb, and (i) Se vs. Au for pyrite formed in the syn-ore stage of the Shuangwang gold deposit.

### 6.2. Source of Sulfur

Sulfur isotopes are often used to indicate the sources of sulfur or metallogenic elements in a deposit [37–40]. The sulfur isotopes in a metal sulfide are controlled by the original material and physical–chemical conditions, including the pH,  $f(\text{O}_2)$ , and the temperature of the hydrothermal fluid [37].

From Table 2, we can see the  $\delta^{34}\text{S}_{\text{V-CDT}}$  values of pyrite in the magmatic rock ranged from 3.8 to 6.1‰ (avg. 4.9‰), demonstrating the characteristics of magmatic sulfur isotope composition ( $\pm 3\%$ , [41]), while that the pyrite in the wallrock near the mine ranged from 4.8 to 13.8‰ (avg. 10.2‰), that in pyrite in the ore ranged from 2.6 to 15.2‰ (avg. 11.1‰), and that in anhydrite in the final stage of mineralization ranged from 24.2 to 26.2‰ (avg. 25.2‰). Overall, the sulfur isotope distribution of pyrite in the ore showed similar characteristics as that in the wallrock near the ore (Figure 8). Therefore, the sulfur in the Shuangwang gold deposit mainly derived from the wall rocks, mixed with the sulfur from magma.

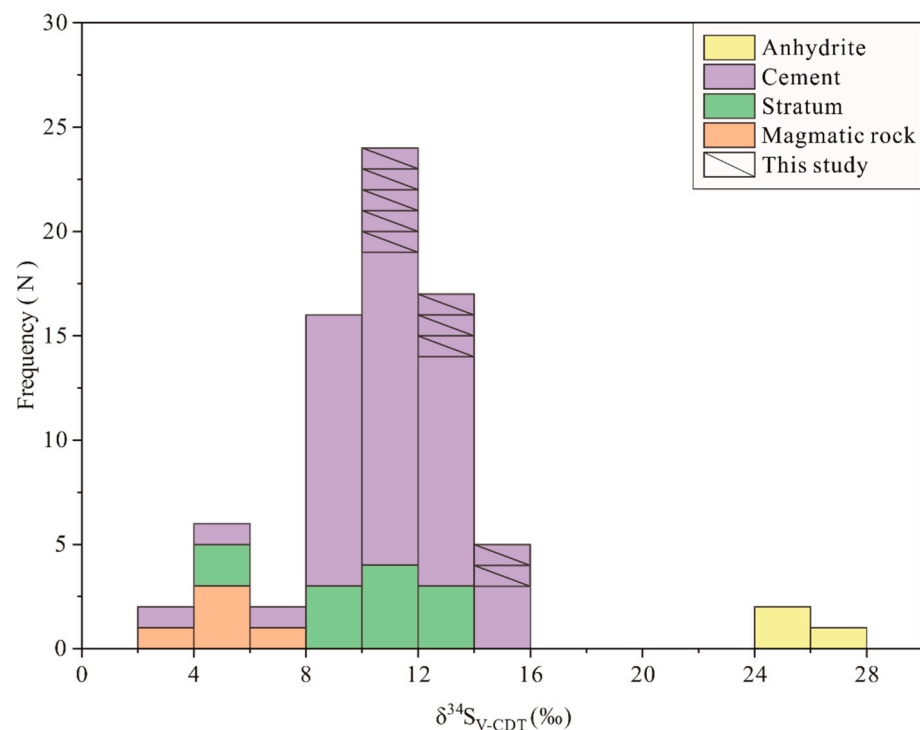


**Figure 8.** Histogram of  $\delta^{34}\text{S}_{\text{V-CDT}}$  isotope compositions from the Shuangwang gold deposit (Data sources: [7,23,24] and this paper).

### 6.3. Discussion on the Genesis of Deposit

Previous studies considering ore-forming fluid have shown that magnesium originated from the wallrock, iron mainly derived from magma [8], the lead isotopic composition has characteristics of the crust and mantle [6,42,43], carbon comes from the strata at great depth [4,6,43], and helium is dominated by crustal fluids [9]. Through this isotope evidence, we can determine that the formation of the considered deposit is related to the strata, deep materials, and even the mantle.

The Xinghohpu Formation has wall rocks with high gold content [23]. The hydrothermal fluid, separated from the magma, extracts elements in the strata during the upward process. Ore-forming elements and sulfur are mainly from the wall rocks. Hydrothermal pressure at the near-surface causes the wallrock to break and to eventually form breccia bodies. Conditional mutation results in the rapid crystallization of pyrite.  $\text{As}^-$  often replaces  $\text{S}^-$  in pyrite, in the form of isomorphism, which promotes gold in the ore-forming fluid to enter the pyrite lattice in the form of solid solution  $\text{Au}^+$  [44]. Gold enters fine-grained

pyrite as invisible gold in a background of high arsenic content. In the later stage, the environment tends to be stable, and the crystal size of pyrite becomes larger; however, there is no gold enrichment, and the arsenic content is also significantly reduced. High arsenic content and rapid crystallization of pyrite may be related to gold mineralization.

## 7. Conclusions

1. Sulfur of the Shuangwang deposit comes from the wallrock, mixed with sulfur from magma.
2. Trace elements were enriched in the syn-ore pyrite much more than in post-ore pyrite.
3. High arsenic content and the rapid crystallization of pyrite are related to gold mineralization.

**Author Contributions:** J.Y., J.L. and X.Y., conceived the ideas; J.Y. and J.L., performed the experiments; J.L., H.H., H.C. and P.Y., processed the data; J.Y., prepared, reviewed and edited the draft. All authors have read and agreed to the published version of the manuscript.

**Funding:** This research was supported by projects of Shaanxi Mineral Resources and Geological Survey (214027160195, 61201506280, and 202001) and Special Fund for Basic Scientific Research of Central Colleges (310827151056, 310827153408, 310827173702 and 300102280401).

**Data Availability Statement:** Not applicable.

**Acknowledgments:** We are grateful to Jianjun Chen and Yinfei Zhang for their field guidance and constructive discussions. Finally, we are grateful to the editors and anonymous reviewers for their valuable suggestions and comments to this manuscript.

**Conflicts of Interest:** The authors declare no conflict of interest.

## References

1. Mao, J.W.; Qiu, Y.M.; Goldfarb, R.J.; Zhang, Z.C.; Garwin, S.; Ren, F.S. Geology, distribution, and classification of gold deposits in the western Qinling belt, central China. *Miner. Depos.* **2002**, *37*, 352–377. [[CrossRef](#)]
2. Chen, Y.J.; Zhang, J.; Zhang, F.X.; Pirajno, F.; Li, C. Carlin and Carlin-like gold deposits in western Qinling Mountains and their metallogenic time, tectonic setting and model. *Geol. Rev.* **2004**, *50*, 134–152.
3. Liu, J.J.; Liu, C.H.; Carranza, E.J.M.; Li, Y.J.; Mao, Z.H.; Wang, J.P.; Wang, Y.H.; Zhang, J.; Zhai, D.G.; Zhang, H.F.; et al. Geological characteristics and ore-forming process of the gold deposits in the western Qinling region, China. *J. Asian Earth Sci.* **2015**, *103*, 40–69. [[CrossRef](#)]
4. Zhang, Z.H.; Mao, J.W.; Li, X.F. Geology, geochemistry and metallogenic mechanism of Shuangwang breccis type gold deposit. *Miner. Depos.* **2004**, *23*, 241–252.
5. Liu, B.Z.; Wang, J.P.; Wang, K.X.; Liu, J.J.; Xie, H.Y.; Cao, R.R.; Hui, D.F.; Cheng, J.J. Characteristics and geological significance of fluid inclusions in the Shuangwang gold deposit, Shaanxi Province. *Geoscience* **2011**, *25*, 1088–1098.
6. Wang, K.X.; Wang, J.P.; Liu, J.J.; Zeng, X.T.; Cao, R.R.; Hui, D.F.; Cheng, J.J.; Zhang, J.L.; Li, Z.G.; Li, X.G.; et al. Geology and stable isotope geochemistry of the Shuangwang gold deposit in Taibai County, Shaanxi Province. *Geol. China* **2012**, *39*, 1359–1374.
7. Wang, J.P.; Liu, J.J.; Carranza, E.J.M.; Liu, Z.J.; Liu, C.H.; Liu, B.Z.; Wang, K.X.; Zeng, X.T.; Wang, H. A possible genetic model of the Shuangwang hydrothermal breccia gold deposit, Shaanxi Province, central China: Evidence from fluid inclusion and stable isotope. *J. Asian Earth Sci.* **2015**, *11*, 840–852. [[CrossRef](#)]
8. Liu, C.H.; Liu, J.J.; Carranza, E.J.M.; Wang, J.P.; Zhai, D.G.; Zhang, F.F.; Wang, Y.H.; Liu, Z.J. Iron and magnesium isotope systematics from the Shuangwang gold deposit in the Qinling Orogen, central China. *Ore Geol. Rev.* **2021**, *134*, 104123. [[CrossRef](#)]
9. Cheng, F. Studies on Material Composition and Genesis of the Shangwang Gold Deposit, Shaanxi Province. Master's Thesis, China University of Geosciences (Beijing), Beijing, China, 1 May 2016.
10. Xie, Y.L.; Xu, J.H.; Qian, D.Y. Characteristics of ore-bearing mineral and its genesis significance of Taibai gold deposit. *J. Univ. Sci. Technol. Beijing* **1997**, *19*, 223–227.
11. Zeng, X.T.; Wang, J.P.; Liu, B.Z.; Liu, C.H.; Cao, R.R.; Gao, C.; Wang, L.; Zhang, G.G.; Zhao, X.J.; Qi, F. Typomorphic characteristics from pyrite of the No. 5 orebody in the Shuangwang Gold Deposit, Shaanxi Province. *Geol. Explor.* **2012**, *48*, 0076–0084.
12. Wang, J.P.; Liu, Z.J.; Liu, J.J.; Zeng, X.T.; Wang, K.X.; Liu, B.Z.; Wang, H.; Liu, C.H.; Zhang, F.F. Trace Element Compositions of Pyrite from the Shuangwang Gold Breccias, Western Qinling Orogen, China: Implications for Deep Ore Prediction. *J. Earth Sci.* **2018**, *29*, 564–572. [[CrossRef](#)]
13. Zhang, G.W.; Meng, Q.R.; Yu, Z.P.; Sun, Y.; Zhou, D.W.; Guo, A.L. Orogenesis and dynamics of Qinling orogen. *Sci. China* **1996**, *26*, 193–200.

14. Dong, Y.P.; Zhang, G.W.; Neubauer, F.; Liu, X.M.; Genser, J.; Hauzenberger, C. Tectonic evolution of the Qinling orogen, China: Review and synthesis. *J. Asian Earth Sci.* **2011**, *41*, 213–237. [[CrossRef](#)]
15. Dong, Y.P.; Santosh, M. Tectonic architecture and multiple orogeny of the Qinling Orogenic Belt, Central China. *Gondwana Res.* **2016**, *29*, 1–40. [[CrossRef](#)]
16. Wang, R.T.; Wang, T.; Gao, Z.J.; Chen, E.H.; Liu, L.X. The main metal deposits metallogenic series and exploration direction in Feng-Tai ore cluster region, Shaanxi Province. *Northwestern Geol.* **2007**, *40*, 77–84.
17. Zeng, Q.T.; McCuaig, T.C.; Hart, C.J.; Jourdan, F.; Muhling, J.; Bagas, L. Structural and geochronological studies on the Liba goldfield of the West Qinling Orogen, Central China. *Miner. Depos.* **2012**, *47*, 799–819. [[CrossRef](#)]
18. Hu, Q.Q.; Wang, Y.T.; Wang, R.T.; Li, J.H.; Dai, J.Z.; Wang, S.Y. Ore-forming time of the Erlihe Pb-Zn deposit in the Fengxian-Taibai ore concentration area, Shaanxi Province: Evidence from the Rb-Sr isotopic dating of sphalerites. *Acta Petrol. Sin.* **2012**, *28*, 258–266.
19. Wang, Y.T.; Chen, S.C.; Hu, Q.Q.; Zhang, J.; Liu, X.L.; Huang, S.K. Tectonic controls on polymetallic mineralization in the Fengxian-Taibai ore cluster zone, Western Qinling, Shaanxi Province. *Acta Petrol. Sin.* **2018**, *34*, 1959–1976.
20. Liu, S.W.; Yang, P.T.; Li, Q.G.; Wang, Z.Q.; Zhang, W.Y.; Wang, W. Indosinian Granitoids and Orogenic Processes in the Middle Segment of the Qinling Orogen, China. *J. Jilin Univ.* **2011**, *41*, 1928–1943.
21. Wang, H. The Features of Magmatic Rocks in Shuangwang Gold Mine, Shaanxi Province and Its Implication on Gold Mineralization. Master's Thesis, China University of Geosciences (Beijing), Beijing, China, 1 May 2012.
22. Zhang, F.; Liu, S.W.; Li, Q.G.; WANG, Z.Q.; Han, Y.G.; Yang, K.; Wu, F.G. LA-ICP-MS Zircon U-Pb Geochronology and Geological Significance of Xiba Granitoids from Qinling, Central China. *Acta Sci. Nat. Univ. Pekin.* **2009**, *45*, 833–840.
23. Liu, C.H. Metallogenic Mechanism and Regularity of the Shuangwang Gold Deposit, Shaanxi Province. Ph.D. Thesis, China University of Geosciences (Beijing), Beijing, China, 1 May 2016.
24. Shi, Z.L.; Liu, J.X.; Fan, S.C. *Geological Characteristics and Genesis of the Shuangwang Gold Deposit, Shaanxi Province*; Shaanxi Science and Technology Press: Xi'an, China, 1989; pp. 1–129.
25. Zong, K.Q.; Klemd, R.; Yuan, Y.; He, Z.Y.; Guo, J.L.; Shi, X.L.; Liu, Y.S.; Hu, Z.C.; Zhang, Z.M. The assembly of Rodinia: The correlation of early Neoproterozoic (ca. 900 Ma) high-grade metamorphism and continental arc formation in the southern Beishan Orogen, southern Central Asian Orogenic Belt (CAOB). *Precambrian Res.* **2017**, *290*, 32–48. [[CrossRef](#)]
26. Hu, Z.C.; Zhang, W.; Liu, Y.S.; Gao, S.; Li, M.; Zong, K.Q.; Chen, H.H.; Hu, S.H. "Wave" Signal-Smoothing and Mercury-Removing Device for Laser Ablation Quadrupole and Multiple Collector ICPMS Analysis: Application to Lead Isotope Analysis. *Anal. Chem.* **2015**, *87*, 1152–1157. [[CrossRef](#)] [[PubMed](#)]
27. Liu, Y.S.; Hu, Z.C.; Gao, S.; Günther, D.; Xu, J.; Gao, C.G.; Chen, H.H. In situ analysis of major and trace elements of anhydrous minerals by LA-ICP-MS without applying an internal standard. *Chem. Geol.* **2008**, *257*, 34–43. [[CrossRef](#)]
28. Bendall, C.; Lahaye, Y.; Fiebig, J.; Weyer, S.; Brey, G.P. In situ sulfur isotope analysis by laser ablation MC-ICPMS. *Appl. Geochem.* **2006**, *21*, 782–787. [[CrossRef](#)]
29. Mason, P.R.D.; Košler, J.; Hoog, J.C.M.; Sylvester, P.J.; Meffan-Main, S. In situ determination of sulfur isotopes in sulfur-rich materials by laser ablation multiplecollector inductively coupled plasma mass spectrometry (LA-MC-ICP-MS). *J. Anal. At. Spectrom.* **2006**, *21*, 177–186. [[CrossRef](#)]
30. Reich, M.; Kesler, S.E.; Utsunomiya, S.; Palenik, C.S.; Chryssoulis, S.L.; Ewing, R.C. Solubility of gold in arsenian pyrite. *Geochim. Cosmochim. Acta* **2005**, *69*, 2781–2796. [[CrossRef](#)]
31. Deditius, A.P.; Utsunomiya, S.; Renock, D.; Ewing, R.C.; Ramana, C.V.; Becker, U.; Kesler, S.E. A proposed new type of arsenian pyrite: Composition, nanostructure and geological significance. *Geochim. Cosmochim. Acta* **2008**, *72*, 2919–2933. [[CrossRef](#)]
32. Large, R.R.; Danyushevsky, L.; Hollit, C.; Maslennikov, V.; Meffre, S.; Gilbert, S.; Bull, S.; Scott, R.; Emsbo, P.; Thomas, H.; et al. Gold and trace element zonation in pyrite using a laser imaging technique: Implications for the timing of gold in orogenic and Carlin-style sediment-hosted deposits. *Econ. Geol.* **2009**, *104*, 635–668. [[CrossRef](#)]
33. Cook, N.J.; Ciobanu, C.L.; Mao, J.W. Textural control on gold distribution in As-free pyrite from the Dongping, Huangtuliang and Hougou gold deposits, North China Craton (Hebei Province, China). *Chem. Geol.* **2009**, *264*, 101–121. [[CrossRef](#)]
34. Tanner, D.; Henley, R.W.; Mavrogenes, J.A.; Holden, P. Sulfur isotope and trace element systematics of zoned pyrite crystals from the El Indio Au-Cu-Ag deposit, Chile. *Contrib. Mineral. Petrol.* **2016**, *171*, 33. [[CrossRef](#)]
35. Deditius, A.P.; Reich, M.; Kesler, S.E.; Utsunomiya, S.; Chryssoulis, S.L.; Walshe, J.; Ewing, R.C. The coupled geochemistry of Au and As in pyrite from hydrothermal ore deposits. *Geochim. Cosmochim. Acta* **2014**, *140*, 644–670. [[CrossRef](#)]
36. Gong, Y.J. The Study on the Tectonic-Fluid System and Metallogenic Mechanism of Shuangwang Gold Deposit in Shaanxi Province. Ph.D. Thesis, China University of Geosciences (Wuhan), Wuhan, China, 1 September 2014.
37. Ohmoto, H. Systematics of Sulfur and Carbon Isotopes in Hydrothermal Ore Deposits. *Econ. Geol.* **1972**, *67*, 551–579. [[CrossRef](#)]
38. Ohmoto, H.; Goldhaber, M.B. Sulfur and carbon isotopes. In *Geochemistry of Hydrothermal Ore Deposits*, 3rd ed.; Barnes, H.L., Ed.; John Wiley and Sons: New York, NY, USA, 1997; pp. 517–611.
39. Seal, R.R. Sulfur Isotope Geochemistry of Sulfide Minerals. *Rev. Mineral. Geochem.* **2006**, *61*, 633–677. [[CrossRef](#)]
40. Sun, C.; Yang, X.Y.; Du, G.F.; Aziz, A.J.H. Genesis of the Selinsing gold deposit, Peninsular Malaysia: Constraints from mineralogy, geochemistry and in situ sulfur isotope compositions of sulfides. *Ore Geol. Rev.* **2019**, *113*, 103111. [[CrossRef](#)]
41. Hoefs, J. *Stable Isotope Geochemistry*, 6th ed.; Springer: Berlin/Heidelberg, Germany, 2009; pp. 1–285. [[CrossRef](#)]

42. Liu, B.Z. Ore-Forming Fluid and Geochemical Characteristics of the No. 5 Ore-Body of the Shuangwang Gold Deposit Shaanxi. Master's Thesis, China University of Geosciences (Beijing), Beijing, China, 1 April 2012.
43. Wang, G.F. Researches on Tectono-Metallogenesis and Metallogenic Prognosis in Shuangwang Gold Deposit, Shaanxi Province, China. Ph.D. Thesis, Central South University, Changsha, China, 1 March 2006.
44. Cabri, L.J.; Newville, M.; Gordon, R.A.; Crozier, E.D.; Sutton, S.R.; McMahon, G.; Jiang, D.T. Chemical speciation of gold in arsenopyrite. *Can. Mineral.* **2000**, *38*, 1265–1281. [[CrossRef](#)]